High-quality curvelet-based motion deblurring from an image pair

Jian-Feng Cai[†], Hui Ji[‡], Chaoqiang Liu[†] and Zuowei Shen[‡]
National University of Singapore, Singapore 117542
Center for Wavelets, Approx. and Info. Proc.[†] and Department of Mathematics[‡]
{tslcaij, matjh, tsllliucq, matzuows}@nus.edu.sg

Abstract

One promising approach to remove motion deblurring is to recover one clear image using an image pair. Existing dual-image methods require an accurate image alignment between the image pair, which could be very challenging even with the help of user interactions. Based on the observation that typical motion-blur kernels will have an extremely sparse representation in the redundant curvelet system, we propose a new minimization model to recover a clear image from the blurred image pair by enhancing the sparsity of blur kernels in the curvelet system. The sparsity prior on the motion-blur kernels improves the robustness of our algorithm to image alignment errors and image formation noise. Also, a numerical method is presented to efficiently solve the resulted minimization problem. The experiments showed that our proposed algorithm is capable of accurately estimating the blur kernels of complex camera motions with low requirement on the accuracy of image alignment, which in turn led to a high-quality recovered image from the blurred image pair.

1. Introduction

When there is a relative motion between the camera and the scene during exposure, the resulted image will appear blurry. This is known as motion blurring in digital imaging. The motion blurring can be modeled by a convolution process:

$$f = g * p + n, \tag{1}$$

where $*$ is the convolution operator, g is the clear image to recover, f is the observed blurred image, p is the blur kernel, and n is the noise. When both g and p are unknowns, how to recover the clear image g from the blurred image is so-called *blind deconvolution* problem. Blind deconvolution is well known as a challenging ill-posed problem, because it is a heavily under-constrained problem with many solutions and it is also sensitive to the noise.

1.1. Previous work

Many research works on general motion deblurring use only a single blurred image. Earlier methods usually (See [18] for more details) require a prior parametric knowledge of the blur kernel p such that the blur kernel can be obtained by only estimating a few parameters. These methods usually only work well on linear motion blur kernels. To remove more complicated blurring from images, a popular approach is to consider a joint minimization model to simultaneously estimate both the blur kernel and the clear image. To overcome the inherent ambiguities between the blur kernel and the clear image, certain regularization terms on both the kernel and the image have to be added in the minimization, e.g., Tikhonov regularization, TV regularization and its variation (*e.g.* [10, 25, 1, 24]). Another interesting approach is to use some probabilistic priors on the image's edge distribution to derive the blur kernel ([15, 19, 17]).

In recent years, many researchers have been working on high-quality motion deblurring using multiple images. Multiple images provide more information of the scene, which can reduce the ill-posedness and the ambiguity of blind motion deblurring. There are two types of multi-image approaches. One is the active approach (computational photography), which actively controls the capturing process using specific hardware to obtain two or more images on the scene for reconstructing the clear image (*e.g.* [2, 27, 23]) Another type of dual-image approach just takes a image pair with different blur kernels or more images as the input:

$$f_1 = g * p_1 + n_1; \quad f_2 = g * p_2 + n_2, \tag{2}$$

where f_1 and f_2 are the observed image pair with the blur kernels p_1 and p_2 respectively. Based on the multi-channel observation framework, the deblurred result is significantly better than that in the single-channel case (*e.g.* [26, 22]) or more sophisticated tasks are allowed ([14, 13]). Similar to single-image deblurring, the optimization-based approach is also proposed to estimate a clear image and two motion-blur kernels from an aligned image pair by solving the fol-

lowing minimization:

$$E(g,p_1,p_2) = \min_{g,p_1,p_2} \sum_{i=1}^{2} \|f_i - p_i * g\|_2^2 + \sum_{i=1}^{2} E_1(p_i) + E_2(g), \quad (3)$$

where $E_1(\cdot)$ is the regularization term on the kernels p_i and $E_2(\cdot)$ is the regularization term on the clear image g. In [11], two images are first aligned manually by the user in Photoshop. Then the minimization problem (3) is formulated in [11] using a regularization term E_1 on the kernel which combining a sparse constraint on p_i and a continuous constraint on the support of the kernel functions p_i.

Impressive results have been shown in [11]. However it requires an accurate image alignment during preprocessing, which is done manually by the user. In practice, the automatic alignment of two blurred images is very challenging, because the appearances of the image can be quite different when it is blurred by different kernels. Even introducing user interactions sometimes is not useful as the geometrical transform between two images can be more complicated than often-used affine transforms. Furthermore, there is still room for further improvements when recovering natural images of complex structures.

1.2. Motivation

The pre-processing of accurate image alignment is very important when our inputs are multiple images taken by a hand-held camera, as the viewpoint always changes when we take pictures. Thus the more realistic model for a blurred image pair (f_1, f_2) is as follows:

$$f_1 = g(h_1(\cdot)) * p_1 + n_1, \quad f_2 = g(h_2(\cdot)) * p_2 + n_2,$$

where h_1 and h_2 is the spatial geometric transform from g to f_i. However, it is observed ([20]) that the alignment error will seriously impact the performance of the blind deblurring, as a small perturbation on the image alignment could bring significant distortions on the estimated blur kernels.

An interesting experiment is done in [20] to show the high sensitivity of the blur kernel estimation to the alignment error in the case of non-blind deconvolution. In the experiment, the clear image g is shown in Fig. 1 (a); and its blurred version f shown in Fig. 1 (b) with the blur kernel p shown in the top right. Then the simulated blurred images used for estimating the blur kernel is obtained by applying a similarity transform on Fig. 1 (b) with different rotations, scales (θ, s)

$$h : \begin{pmatrix} x \\ y \end{pmatrix} \longrightarrow s \begin{pmatrix} \cos\theta & \sin\theta \\ -\sin\theta & \cos\theta \end{pmatrix} \begin{pmatrix} x \\ y \end{pmatrix} \quad (4)$$

Then the blur kernel $\widetilde{p}$ under such an alignment error is estimated by solving the following equation

$$\widetilde{f} = g * \widetilde{p}, \quad \text{where } (\widetilde{f}) = g(h(\cdot)) * p$$

(a) clear image (b) blurred image

Figure 1. (a) is the clear image; (b) is the blurred image without alignment perturbation, the blur kernel shown in the top rightmost.

$[-1.4^\circ, 0.98]$ $[-0.7^\circ, 0.99]$ $[0^\circ, 1.00]$ $[0.7^\circ, 0.99]$ $[1.4^\circ, 0.98]$

Figure 2. The images in the top row are the blur kernel estimated using the blurred image (b) and a number of clear images (a) after a small alignment perturbation of different rotation and scale. Two numbers in brackets under each kernel are the rotation angle and scale value (θ, s). All images are from [20].

using a least squares minimization with Tikhonov regularization. It is noted that the multi-image blind blurring is not sensitive to small translations between two images, as the translation between two images only results in a shift on the estimated kernel. Fig 2 showed that the blur kernel is very sensitive to even a small alignment error for the case of non-blind deblurring. As a more ill-posed problem, blind motion deblurring is even more sensitive to the alignment error. The experiment above clearly indicated the importance of the robustness to the alignment error when developing dual-image blind motion deblurring techniques.

2. Our work

The goal of this paper is to develop an efficient numerical algorithm to recover a high-quality clear image from an image pair, which are very robust to the alignment error between the image pair. It is noted that our approach does not address the problem of image alignment for blurred images. Instead, our work focuses on alleviating the alignment error and other model errors by using good prior information on the motion-blur kernels. By greatly lowering the requirement on the image alignment, our work can also be applied on removing motion blurring in videos. In other words, we take the image pair $\{\widetilde{f}_1, \widetilde{f}_2\}$ without accurate image alignment as the input:

$$\widetilde{f}_1(\vec{r}) = f_1(\vec{r} + \epsilon_1(\vec{r})), \quad \widetilde{f}_2(\vec{r}) = f_1(\vec{r} + \epsilon_2(\vec{r})), \quad (5)$$

where f_1 and f_2 are defined in (2), $\vec{r}$ is the image coordinates, and $\epsilon_1(\vec{r})$ and $\epsilon_2(\vec{r})$ are the image alignment errors. The goal is to develop a numerical algorithm to estimate g and p_i, which are robust to both alignment error ∇h_i

and image formation noise n_i. As the blind motion deblurring is an ill-posed problem, some prior on the kernel has to be imposed for a better constraint. A typical motion blur p can be expressed as

$$p = v(x, y)|_\Omega, \tag{6}$$

where v is the speed and Ω is the motion path. In other words, the blur kernel is a smooth (or piecewise smooth) function with the support of a smooth curve in $\mathbb{R}^2$.

Inspired by the recent progress in sparse approximation using redundant systems, we believe that the sparsity of the kernel function under certain redundant domains is a very powerful constraint on the blur kernel. Our study shows that the motion-blur kernel of type (6) in the redundant *curvelet* system ([8]) will have an extremely sparse representation. Thus, we propose a sparsity constraint on the kernel, which is based on the ℓ_1 norm of the curvelet coefficients of the function. Moreover, the curvelet system is also a *tight frame* system ([12]) which allows the perfect reconstruction from the curvelet coefficients of the function to the original function. The perfect reconstruction property of the curvelet system allows the applications of some new numerical algorithms to efficiently solve the resulting minimization.

The sparsity constraint on the blur kernel is not a completely new idea. [15] used an approximate ℓ_0 norm on the function values of the blur kernel as the measurement on the sparsity of the kernel. Such a sparsity constraint could prevent the support of the kernel from being too large. However, it does not characterize the continuous "curvy" geometrical property of the support Ω of the blur kernel, which could leads to too sparse solution of only a few isolation dots ([11]). [11] addressed this issue by adding an ad-hoc anisotropic diffusion procedure when estimating the blur kernel to avoid the solution with a discontinuous support.

Our curvelet-based sparsity constraint has a couple of advantages over these regularization models.

1. Under the curvelet system, the blur kernel of type (6) has the sparsest solution among all known representations ([8]). The resulting minimization benefits greatly from such an optimal sparsity, as it increases the robustness to the noise and on the alignment error.

2. Our sparsity constraint is based on the ℓ_1 norm of the kernel in the curvelet domain. Because the curvelet system is a tight frame system with the property of perfect reconstruction, a new minimization technique called *linearized Bregman iteration* ([6]) is applicable to the resulting minimization problem, which is empirically much faster than other standard non-linear techniques (e.g. interior point method) do ([5]), especially when solving large-scale ℓ_1 norm related minimization problems.

The rest of the paper is organized as follows. In Section 3, we formulate our minimization strategy and explain its underlying motivation. In Section 4, we present the numerical algorithm to solve the proposed minimization problem. Section 5 is devoted to the experimental evaluation and the discussion.

3. Problem formulation and its analysis

In our formulation, we take the following two misaligned blurred images $\{\widetilde{f}_1, \widetilde{f}_2\}$ as the input:

$$\widetilde{f}_1(\vec{r}) = g(\vec{r}+\epsilon_1(\vec{r}))*p_1+n_1,\ \widetilde{f}_2(\vec{r}) = g(\vec{r}+\epsilon_2(\vec{r}))*p_2+n_2, \tag{7}$$

where g is the clear image, $\vec{r}$ and $\epsilon(\vec{r})$ are the image coordinates and the alignment error respectively, p_1 and p_2 are the blur kernels, and n_1 and n_2 are the image noises. We propose an alternative minimization method to simultaneously estimating the blur kernels p_1, p_2 and the clear image g. Before we introduce our formalization on the new minimization model, we give a brief review of the curvelet. More details can be found in [8, 7, 9].

3.1. Curvelet system and the blur kernel

The curvelet system can be viewed as the generalization of the wavelet system to better characterize the discontinuities across the curves in $\mathbb{R}^2$. The curvelet system is designed to represent smooth curves by a small number of coefficients, as the basic elements in the curvelet system exhibit high directional sensitivity and high anisotropy.

Let us define a set of generator functions which are multiple rotated versions of a given function ψ:

$$\Psi := \{\psi_{\ell,j,k_1,k_2} = \psi(2^j R_{\theta_\ell}((x, y)^T - x_{\ell,j,k_1,k_2}))\} \tag{8}$$

Then the curvelet system is defined as the collection of the dilations and shifts of Ψ:

$$x_{\ell,j,k_1,k_2} = R^{-1}_{\theta_\ell}(2^{-j}k_1, 2^{-j/2}k_2)^T, \quad j, k_1, k_2 \in \mathbb{Z},$$

where $\theta_\ell = 2\pi 2^{\lfloor j \rfloor}\ell$ is the equi-spaced sequence of rotation angles such that $0 \le \theta_\ell < 2\pi$, R_θ is the rotation by θ radians and R^{-1}_θ its inverse. See Fig. 3 for the illustration of the curvelets and a two-level decomposition.

It is noted that the scaling in the curvelet system is a parabolic scaling such that the system is well localized in space and obeys approximately the relationships: length $\approx 2^{-j}$, width $\approx 2^{-2j}$. Therefore, the length and the width of a curvelet obey the anisotropic scaling relation: $width \approx length^2$. Moreover, the curvelets are directional sensitive as they are oriented in the co-direction $\theta_J = \pi\ell 2^{-j}$ with the scale 2^{-2j}; that is, # orientations $= 1/\sqrt{\text{scale}}$. The combination of the parabolic scaling and the directional sensitivity give a very sparse presentation for singularities along curves or hypersurfaces in the image.

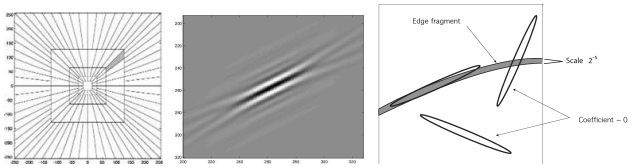

(a) (b) (c)

Figure 3. (a) The two-level decomposition. (b) One curvelet. (c) A bandpass curve fragment together with three curvelets. All images are from [7].

The curvelet system is also a *tight frame* in $L_2(\mathbb{R}^2)$ which allows a perfect reconstruction:

$$f = \sum_{\ell,j,k_1,k_2} \langle f, \psi_{\ell,j,k_1,k_2}\rangle \psi_{\ell,j,k_1,k_2}, \quad \forall f \in L^2(\mathbb{R}), \quad (9)$$

where $\langle \cdot, \cdot \rangle$ is the inner product of $L^2(\mathbb{R})$. The set of all inner products $\{v_{\ell,j,k_1,k_2} = \langle f, \psi_{\ell,j,k_1,k_2}\rangle\}$ with ψ_{ℓ,j,k_1,k_2} defined in (8) are called the*curvelet coefficients* of f. An orthonormal basis is a tight frame, hence a tight frame is a generalization of an orthonormal basis. However, tight frames sacrifice the orthogonality and the linear independence of the system in order to get more flexibility. Tight frames can be redundant.

In the 2D discrete case, the discrete curvelet transform is a linear transform on the given discrete input, by thinking of the output as a collection of coefficients obtained from the digital analog to the inner product in (9). We denote an $n \times n$ image f as a vector $\mathbf{f} \in \mathbb{R}^N, N = n^2$ by concatenating all columns of the image. Then, the discrete version of the curvelet transform is

$$\mathbf{v} = \mathcal{A}\mathbf{f},$$

where $\mathcal{A} \in \mathbb{R}^{K \times N}$. The discrete version of the perfect reconstruction formula (9) can be expressed as

$$\mathbf{f} = \mathcal{A}^T \mathbf{v}.$$

It is equivalent to say that, in matrix form, $\mathcal{A}$ is a tight frame if and only if $\mathcal{A}^T\mathcal{A} = I$ (See [4] for more details). Unlike the orthonormal case, we emphasize that $\mathcal{A}\mathcal{A}^T \neq I$ in general. In the implementation, there exist efficient algorithms for the curvelet decomposition and reconstruction ([7]).

3.2. Joint minimization using sparsity priors

Let $\mathbf{f}_1, \mathbf{f}_2 \in \mathbb{R}^{n^2}$ denote a pair of blurred images f_1, f_2 after column concatenation. In our implementation of Algorithm 1, we assume that the support of the blur kernel is also of size no larger than $n \times n$ and let $\mathbf{p}_1, \mathbf{p}_2 \in \mathbb{R}^{n^2}$ denote the two blur kernel functions p_1, p_2 after column concatenation. Let "$\otimes$" denote the convolution operator of p and f after concatenating operation:

$$p * f = \mathbf{p} \otimes \mathbf{f}.$$

Let $\mathbf{v}_i = \mathcal{A}\mathbf{p}_i, i = 1, 2$ denote the curvelet coefficients of the two blur kernels $\mathbf{p}_1, \mathbf{p}_2$. we formulate the dual-image blind motion deblurring problem as

$$\underset{\mathbf{g},\mathbf{v}_1,\mathbf{v}_2}{\operatorname{argmin}} \sum_{i=1}^{2} \|\mathbf{g} \otimes (\mathcal{A}^T\mathbf{v}_i) - \mathbf{f}_i\|_2 + \lambda_1 \sum_{i=1}^{2} \|\mathbf{v}_i\|_1 + \lambda_2 E(\mathbf{g}) \quad (10)$$

where λ_1, λ_2 are some regularization parameters, $E(\mathbf{g})$ is the image regularization term which we will give more details in the later discussion.

In the optimization formulation (10), besides the regularization term of the image and the fidelity term between the yielded solution and the observed image, the objective function (10) is to minimize the ℓ_1 norm of the curvelet coefficients of two blur kernels, which equivalently is to maximize the sparsity of two blur kernels under the curvelet system. In summary, our optimization strategy is among all solutions which have a reasonable good ℓ_2 norm approximation to the given blurred images, we are seeking for the sparsest solution of two blur kernels in the curvelet domain.

The regularization term $E(g)$ in (10) allows to vary in our approach. In most iterations in our solver, we use an ℓ_2 norm on the image derivatives $E(\mathbf{g}) = \|\nabla\mathbf{g}\|_2^2$, instead of using TV regularization $E(\mathbf{g}) = \|\nabla\mathbf{g}\|_1$. The main reason is for the efficiency of solving the resulting minimization. It is known that the ℓ_1 norm regularization is much more computationally expensive than the ℓ_2 norm regularization. Meanwhile, it is observed in our study that before the two estimated blur kernels begin to approximate the true solution quite well, there is essentially no difference between using ℓ_1 norm and using ℓ_2 norm on the image gradients. In other words, there are not much benefits of using ℓ_1 norm before obtaining accurate blur kernels. Therefore, when we iteratively solve the minimization (10), we use $E(\mathbf{g}) = \|\nabla\mathbf{g}\|_2^2$. After stopping the iteration, we switch to more advanced non-blind technique to recover the clear image using estimated blur kernels.

In a quick glance, the minimization (10) is a very challenging large-scale minimization problem. However, there exists a newest technique which can be applied to solve our proposed minimization problem This new technique is called *linearized Bregman iteration* ([5, 6]). It is observed in many applications that the linearized Bregman iteration is much more efficient than other popular non-linear minimization techniques (e.g. interior point method) when solving large-scale ℓ_1 norm related minimization problems with millions of unknowns. In the next section, we will develop an efficient numerical scheme based on this new technique.

4. Numerical algorithm

The minimization problem (10) is a joint minimization problem on the curvelet coefficients $\mathbf{v}_1, \mathbf{v}_2$ and the image $\mathbf{g}$.

In practice, the alignment error and image noise may lead to a solution which is against the basic rules of the image and the kernel. In order to obtain a sound solution, we chose to impose the non-negative constraint on the image $\mathbf{g}, \mathbf{p}_i$ and normalization constraint on $\mathbf{p}_i$:

$$\begin{cases} \mathbf{p}_i \geq 0, \quad \sum_j \mathbf{p}_i(j) = 1, \quad i = 1, 2. \\ \mathbf{g} \geq 0. \end{cases} \tag{11}$$

We need to solve $\mathbf{p}_1, \mathbf{p}_2$ and $\mathbf{g}$ from the joint minimization problem (10). (10) is known as a very challenging minimization problem. The commonly used heuristic method for solving such a minimization problem is the alternative minimization approach; see [10] for instance. Let $[\mathbf{p}]_*$ denote the matrix form of convolution operator by the kernel $\mathbf{p}$. Algorithm 1 outlines the alternative minimization algorithm for (10).

There are only two non-trivial steps in Algorithm 1. One is solving (14). The direct solution of (14) is given by

$$\Big(\sum_{i=1}^{2} \lambda_i [\mathbf{p}_i^{(k)}]_*^T [\mathbf{p}_i^{(k)}]_* + \Delta\Big)^{-1} \Big(\sum_{i=1}^{2} \lambda_i [\mathbf{p}_i^{(k)}]_*^T \mathbf{f}_i\Big) \tag{12}$$

for some parameter λ_i, and Δ is the Laplacian. (12) can be efficiently calculated by using DCT ([21]). Therefore, in Algorithm 1, the only challenging task is to solve (13), which could be very computationally expensive. In the next section, we will present an efficient algorithm to solve this minimization problem.

Based on the linearized Bregman iteration technique ([6]), an efficient solver is available to find a good approximate solution to (13) during each iteration of Algorithm 1. See Algorithm 2 for the detailed description on our solver for the minimization problem (13).

It was proved in [5] that $\mathbf{w}^{(l)}$ generated by (15) converges to the unique solution of

$$\begin{array}{ll} \min\limits_{\mathbf{v}} & \|\mathbf{v}\|_1 + \frac{1}{2\mu\nu}\|\mathbf{v}\|_2^2 \\ \text{subject to} & [\mathbf{g}^{(k+1)}]_*(\mathcal{A}^T\mathbf{v}) = \mathbf{f}_i. \end{array} \tag{18}$$

Though (18) is not exactly (13), it was shown in [5] that $\mathbf{w}^{(l)}$ of the iteration (15) leads to a good approximation of a solution of (13), if we choose a sufficiently large μ and stop (15) early whenever

$$\|[\mathbf{g}^{(k+1)}]_*(\mathcal{A}^T\mathbf{w}^{(l)}) - \mathbf{f}_i\|_2 \leq \delta.$$

Usually, it takes only a few iterations for (15) to get an approximate solution of (13).

5. Experimental Evaluation and discussion

Through all our experiments, λ_2 in (14) is set as 0.001 and λ in (17) is set as 0.001. The initial $\mathbf{g}^{(0)}$ is either $\mathbf{f}_1$ or $\mathbf{f}_2$. The parameters in (15) is chosen as $\mu = 0.2$ and $\nu = 1$. We found empirically that only 1 iteration of Algorithm 2 is needed to give very good sparse kernels, and 200 iterations are done in Algorithm 1 before it stops.

Algorithm 1 Alternative minimization algorithm

1. Let $\mathbf{g}^{(0)}$ be the initial guess.
2. Iterate on k until convergence.
   (a) Given the image $\mathbf{g}^{(k)}$, solve (10) with respect to $\mathbf{p}_1$ and $\mathbf{p}_2$, i.e., for each $\mathbf{p}_i$, i=1,2, set $\mathbf{v}_i^{(k+1)}$ be a solution of
   $$\min_{\mathbf{v}_i} \|[\mathbf{g}^{(k)}]_*(\mathcal{A}^T\mathbf{v}_i) - \mathbf{f}_i\|_2 + \lambda_1\|\mathbf{v}_i\|_1 \tag{13}$$
   Then impose the physical constraint:
   $$\mathbf{p}_i^{(k+1/2)} = \begin{cases} \mathcal{A}^T\mathbf{v}_i^{(k+1)}(j), & \text{if } \mathcal{A}^T\mathbf{v}_i^{(k+1)}(j) \geq 0, \\ 0, & \text{otherwise,} \end{cases}$$
   followed by the normalization
   $$\mathbf{p}_i^{(k+1)} := \mathbf{p}_i^{(k+1/2)} / \|\mathbf{p}_i^{(k+1/2)}\|_1.$$
   (b) Given the blur kernels $\mathbf{p}_1^{(k+1)}$ and $\mathbf{p}_2^{(k+1)}$, solve (10) with respect to $\mathbf{g}$, i.e., set $\mathbf{g}^{(k+1/2)}$ be a solution of
   $$\min_{\mathbf{g}} \sum_{i=1}^{2} \|[\mathbf{p}_i^{(k+1)}]_*\mathbf{g} - \mathbf{f}_i\|_2 + \lambda_2\|\nabla\mathbf{g}\|_2^2 \tag{14}$$
   Then enhancing the physical constraint:
   $$\mathbf{g}^{(k+1)}(j) = \begin{cases} \mathbf{g}^{(k+1/2)}(j), & \text{if } \mathbf{g}^{(k+1/2)}(j) \geq 0 \\ 0, & \text{otherwise.} \end{cases}$$
3. Given the two kernels $\mathbf{p}_1^*$ and $\mathbf{p}_2^*$ from Step 2, recover the ultimate clear image $\mathbf{g}^*$ by the non-blind deconvolution technique provided in [5].

(a) (b) (c)

Figure 4. (a) The original clear image. (b) One blurred image. (c) Another blurred image. The corresponding blur kernels are shown on the top left of the images respectively.

5.1. Simulated images

In the first experiment, we would like to see how robust the estimation of motion blur kernels in our proposed method is to the alignment error. The images used in this experiment are synthesized as follows. Two blurred images

Algorithm 2 Algorithm for solving (13)

1. Define $\mathbf{w}^{(0)} = \mathbf{u}^{(0)} = \mathbf{0}$,

2. Iterate on $\ell = 0, 1, \cdots$, until $\|[\mathbf{g}^{(k)}]_* \mathcal{A}^T \mathbf{w}^{(\ell)} - f_i\| \leq \delta$:

$$\begin{cases} \mathbf{u}^{(l+1)} = \mathbf{u}^{(l)} - \mathcal{A} G^{(k)} \\ \qquad\qquad [\mathbf{g}^{(k)}]_*^T \Big([\mathbf{g}^{(k)}]_* (\mathcal{A}^T \mathbf{w}^{(l)}) - \mathbf{f}_i \Big), \\ \mathbf{w}^{(l+1)} = \nu T_\mu(\mathbf{u}^{l+1}), \end{cases} \tag{15}$$

where T_μ is the soft-thresholding operator defined by

$$\begin{aligned} &T_\mu(\mathbf{u}) = [t_\mu(u_1), t_\mu(u_2), \ldots], \\ &\text{with} \quad t_\mu(u_i) = \text{sign}(u_i) \max(|u_i| - \mu, 0), \end{aligned} \tag{16}$$

and $G^{(k)}$ is a preconditioning matrix

$$G^{(k)} = \left([\mathbf{g}^{(k)}]_*^T [\mathbf{g}^{(k)}]_* + \lambda \Delta \right)^{-1}. \tag{17}$$

3. $\mathbf{v}_i^{(k+1)} = \mathbf{w}^\ell$ from Step 2.

(Fig. 4 (b) and (c)) are generated by applying two different blur kernels on the original image (Fig. 4 (a)) respectively. The alignment error is simulated by applying a similarity transform (4) on Fig. 4 (c) with different rotations and scales (θ, s) and the same translation. The values of the translation is set to $(5, 5)$ pixels in the experiment. Our proposed method is applied on each pair of the blurred image in Fig. 4 (b) and transformed blurred images from Fig. 4 (c) without any image alignment. Fig. 5 (a) show the estimated motion blur kernels from our method with respect to different alignment errors.

The results shown in Fig. 5 (a) clearly demonstrated that our method is capable of finding complicated blur kernels and is robust to the alignment error. For the comparison, we also estimated the blur kernels by least squares minimization with Tikhonov regularization. Fig. 5 (b) showed that the routine approach cannot identify the motion blur kernel even there is little alignment error.

Fig. 6 (b)-(d) show the deblurred images using our method with various alignment errors. As the comparison, Fig. 6 (a) showed the deblurred image by using Tikhonov regularization in the case of no image alignment error.

In the second experiment, we would like to evaluate the robustness of our method to image noise. All blurred images in this experiment are generated by applying two blur kernels on the original image, subsequently contaminated by zero mean white noise with different noise levels. Thirty two random samples are generated for each noise level. The noise level is measure by the so-called *SNR* (signal to noise

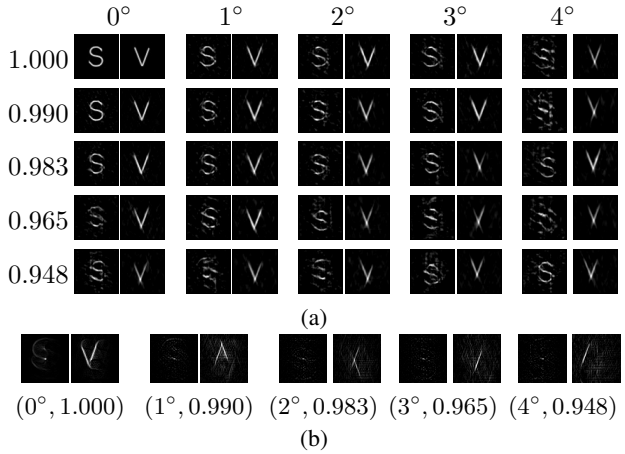

Figure 5. (a) The kernels of the images in Fig. 4 (b)-(c) estimated by our method. The horizontal vector on the top is the rotation angle θ, and the vertical vector on the left is the scales s with respect to applied spatial transforms. (b) The kernels of the images in Fig. 4 (b)-(c) estimated by Tikhonov regularization. Two numbers in brackets above each pair of kernels are the rotation angle and scale of the corresponding spatial transform.

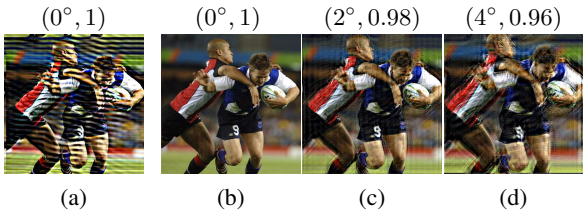

Figure 6. (a) the deblurred image by the kernel estimated from Tikhonov regularization. Two numbers in brackets on the top of each deblurred image are the rotation angle and scale. (b)-(d) are the deblurred images using estimated kernels from our approach.

ratio) of the noised image $\widetilde{I}$ to the clean image I defined as

$$\text{SNR}(\widetilde{I}) = 20 \log_{10} \|I\|_2 / \|I - \widetilde{I}\|_2.$$

Fig. 7 shows that the estimation of the blur kernel by our method is also very robust to the image noise. From the experiments, we also see that the alignment error is far more

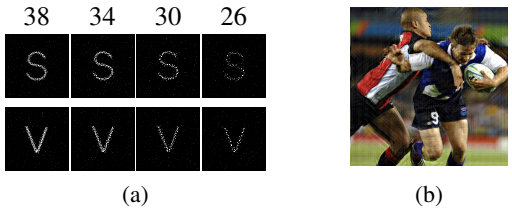

Figure 7. (a) The estimated kernels of Fig. 4 (b)–(c) for various noise levels. The vector on the top is the value of SNRs. (b) The de-blurred image from noisy images with SNR= 26dB.

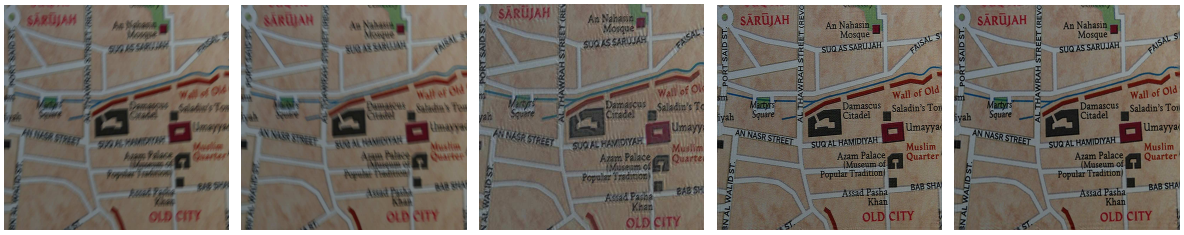

(a) (b) (c) (d) (e)

Figure 8. (a)–(b): two blurred images; (c): the deblurred image using Fergus *et al.*'s method ([15]); (d): the deblurred image using Chen *et al.*'s method ([11]); (e): the deblurred image using our method.

(a) (b) (c) (d) (e)

Figure 9. (a)–(b): two blurred images; (c): the deblurred image of (a) using Fergus *et al.*'s method ([15]); (d): the deblurred image using Chen *et al.*'s method ([11]); (e): the deblurred image using our method.

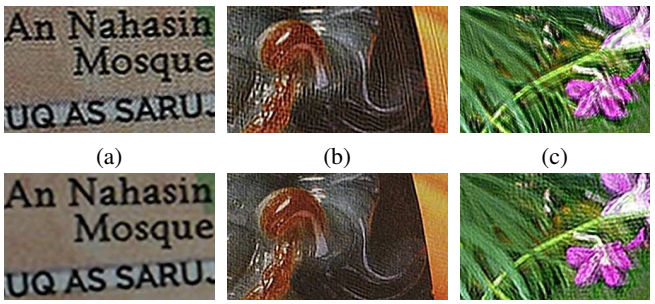

(a) (b) (c)

(d) (e) (f)

Figure 11. (a)–(c): a region of Fig. 8 (d)–Fig. 10 (d) by Chen *et al.*'s method ([11]); (d)–(f): a region of Fig. 8 (e)–Fig. 10 (e) by Our method.

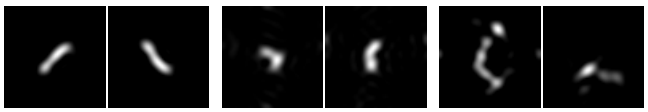

(a) (b) (c) (d) (e) (f)

Figure 12. The estimated blur kernels for blurred image pairs in Fig. 8–10 using our algorithm. (a)–(b): the kernels for Fig. 8 (a)–(b); (c)–(d): the kernels for Fig. 9 (a)–(b); (e)–(f): the kernels for Fig. 10 (a)–(b).

serious than image formation noise.

5.2. Real images

We also tested our method on real images. All images are taken by a hand-held commodity video camera. The images are first automatically aligned by using the conventional method from [3] before applying our method. The tested images are restored by our proposed method and are compared against the results from the method of Fergus *et al.* [15] and of Chen *et al.* [11]. Fig. 8–9 show that the blurred image pair and the results from all three methods. Clearly, the methods using an image pair are superior than the single-image method. The visual quality of recovered images using our method and the method of Chen *et al.* [11] are much better than that of using the method of Fergus *et al.* [15]. The performance gap between Chen *et al.*'s method and ours is smaller. However, the improvement of our method is still noticeable. See Fig. 11 for the comparison between our results and theirs after zooming in.

5.3. Conclusion

Using a pair of images of the same scene greatly improves the visual quality of the recovered clear image. Based on the extremely sparse representation of the motion-blur kernel function using the redundant curvelet system, we propose a new sparsity regularization strategy on the blur kernel such that the resulting minimization model is robust to image noise and, more importantly, to the image alignment error. Moreover, the perfect reconstruction property of the curvelet system gives a fast algorithm to solve

(a) (b) (c) (d) (e)

Figure 10. (a)–(b): two blurred images; (c): the deblurred image of (a) using Fergus *et al*.'s method ([15]); (d): the deblurred image using Chen *et al*.'s method ([11]); (e): the deblurred image using our method.

the resulting minimization efficiently. Our experiments on both synthesized images and real images showed that our method can recover a high-quality image from a blurred image pair with minimal requirement on the image alignment pre-processing.

ACKNOWLEDGMENTS

The authors would like to thank the anonymous reviewers for very helpful comments and suggestions. This work is partially supported by various NUS ARF grants. The first and the thirds author also would like to thank DSTA funding for support of the programme "Wavelets and Information Processing".

References

[1] L. Bar, B. Berkels, M. Rumpf, and G. Sapiro. A variational framework for simultaneous motion estimation and restoration of motion-blurred video. In *ICCV*, 2007.

[2] M. Ben-Ezra and S. K. Nayar. Motion-based motion deblurring. *IEEE Trans. PAMI*, 26(6):689–698, 2004.

[3] J. Bergen, P. Anandan, K. Hanna, and R. Hingorani. Hierarchical model-based motion estimation. In *ECCV*, 1992.

[4] J.-F. Cai, R. Chan, and Z. Shen. A framelet-based image inpainting algorithm. *Appl. Comput. Harmon. Anal.*, 24:131–149, 2008.

[5] J.-F. Cai, S. Osher, and Z. Shen. Linearized bregman iterations for frame-based image deblurring. *SIAM J. Imaging Sci.*, 2(1):226–252, 2009.

[6] J.-F. Cai, S. Osher, and Z. Shen. Linerarized bregman iterations for compressed sensing. *Math. Comp.*, to appear.

[7] E. Candes, L. Demanet, D. L. Donoho, and L. Ying. Fast discrete curvelet transforms. *Multiscale Model. Simul.*, 5:861–899, 2005.

[8] E. Candes and D. L. Donoho. New tight frames of curvelets and optimal representations of objects with piecewise-C^2 singularities. *Comm. Pure Appl. Math*, 57:219–266, 2002.

[9] E. Candes and M. Wakin. An introduction to compressive sampling. *IEEE Sign. Proc. Mag.*, 25(2):21–30, 2008.

[10] T. F. Chan and C. K. Wong. Total variation blind deconvolution. *IEEE Tran. Image Processing*, 7(3):370–375, 1998.

[11] J. Chen, L. Yuan, C. K. Tang, and L. Quan. Robust dual motion deblurring. In *CVPR*, 2008.

[12] I. Daubechies, B. Han, A. Ron, and Z. Shen. Framelets: MRA-based constructions of wavelet frames. *Appl. Comput. Harmon. Anal.*, 14:1–46, 2003.

[13] P. Favaro, M. Burger, and S. Soatto. Scene and motion reconstruction from defocused and motion-blurred images via anisotropic diffusion. In *ECCV*, pages 257–269, 2004.

[14] P. Favaro and S. Soatto. A variational approach to scene recognition and image segmentation from motion-blur cues. In *CVPR*, volume 1, pages 631–637, 2004.

[15] R. Fergus, B. Singh, A. Hertzmann, S. T. Roweis, and W. T. Freeman. Removing camera shake from a single photograph. In *SIGGRAPH*, volume 25, pages 783–794, 2006.

[16] H. Ji and C. Q. Liu. Motion blur identification from image gradients. In *CVPR*, pages 1–8, 2008.

[17] J. Jia. Single image motion deblurring using transparency. In *CVPR*, pages 1–8, 2007.

[18] D. Kundur and D. Hatzinakos. Blind image deconvolution. *IEEE Signal Processing Magazine*, 12:43–46, 1996.

[19] A. Levin. Blind motion deblurring using image statistics. In *NIPS*, pages 841–848, Dec. 2006.

[20] Y. Lu, J. Sun, L. Quan, and H. Shum. Blurred/non-blurred image alignment using kernel spareness prior. In *ICCV*, 2007.

[21] M. K. Ng, R. H. Chan, and W. Tang. A fast algorithm for deblurring models with neumann boundary condition. *SIAM J. Sci. Comput.*, 21(3):851–866, 2000.

[22] G. Panci, P. Campisi, S. Colonnese, and G. Scarano. Multichannel blind image deconvolution using the bussgang algorithm: spatial and multiresolution approaches. *IEEE Trans. Image Processing*, 12:1324–1337, 2003.

[23] R. Raskar, A. Agrawal, and J. Tumblin. Coded exposure photography: Motion deblurring via fluttered shutter. In *SIGGRAPH*, volume 25, pages 795–804, 2006.

[24] Q. Shan, J. Jia, and A. Agarwala. High-quality motion deblurring from a single image. In *SIGGRAPH*, 2008.

[25] Q. Shan, W. Xiong, and J. Jia. Rotational motion deblurring of a rigid object from a single image. In *ICCV*, 2007.

[26] M. Sorel and J. Flusser. Space-variant restoration of images degraded by camera motion blur. *IEEE Trans. Image Processing*, 17:105–116, 2008.

[27] Y. Tai, H. Du, M. S. Brown, and S. Lin. Image/video deblurring using a hybrid camera. In *CVPR*, 2008.